Exploring multicomponent eutectic alloys along an univariant eutectic line

Xi Jin [a], Zan Xue [a], Zhouzhu Mao [a], Ruipeng Guo [a], Xuejiao Wang [a], Xiaohui Shi [a], Shaochun Yin [a], Min Zhang [a], Peter K. Liaw [b], Junwei Qiao [a, c] *

[a] College of Materials Science and Engineering, Taiyuan University of Technology, Taiyuan 030024, China

[b] Department of Materials Science and Engineering, The University of Tennessee, 37996–2200 Knoxville, TN, USA

[c] Key Laboratory of Interface Science and Engineering in Advanced Materials, Ministry of Education, Taiyuan University of Technology, Taiyuan, 030024, China

* Corresponding author: Junwei Qiao. E-mail address: qiaojunwei@gmail.com

Abstract: Multicomponent eutectic alloys (MCEAs) have attracted broad attention due to the excellent castability as well as mechanical properties. Till now, disordered face-centred-cubic (FCC)/disordered body-centred-cubic (BCC)-structured MCEA has been absent. In this work, we propose a route to design MCEAs along the univariant eutectic line. On the basis of this, four FCC/BCC-structured MCEAs with similar lamellar microstructures but different

tensile properties have been designed and successfully prepared. The yield-strength difference is found mainly results from the strength difference of the FCC matrix, while the BCC/FCC strength ratio R^* accounts for the strain-hardening capability difference. The current work is helpful for exploring novel MCEAs with excellent mechanical properties.

1. Introduction

In 2004, Cantor et al.[1] put forward the concept of multicomponent alloys (MCEAs) and attempted to investigate the unexplored central region of multicomponent alloy phase space. At the meantime, Yeh et al.[2] proposed the concept of high entropy alloys (HEAs), which contain five or more principal elements with concentration of each element between 5 - 35 atomic percent (at.%). The high mixing entropy values of MCEAs or HEAs promote the stability of solid solution phases and restrain the formation of intermetallic compounds. Till now, large amount of HEAs with single or dual phases have been designed and prepared successfully, some of which exhibit much better performances than traditional alloys. For instance, a single-phase face-centred-cubic (FCC) CoCrFeMnNi HEA has exceptional fracture-resistant at cryogenic temperature[3], while a single-phase body-centred-cubic (BCC) refractory like MoNbTaW and MoNbTaVW HEAs possess excellent mechanical strength (400 MPa) at ultrahigh temperatures up to 1,600°C[4]. Recently, it has been reported that the refractory $Hf_{0.5}Nb_{0.5}Ta_{0.5}Ti_{1.5}Zr$ HEA exhibits much better corrosion resistance than Ti

alloy in the 3.5 weight percent (wt.%) NaCl solution due to the unusually high pitting potential value of + 8.36 V[5].

On account of the large number and content of principal elements, the majority of HEAs present inferior castability and subsequent compositional segregation and non-uniformity for mechanical properties, which limits the engineering applications. Dual-phase eutectic high entropy alloys (EHEAs) or multicomponent eutectic alloys (MCEAs) perfectly overcome the above challenge by drastically narrowing the temperature interval of the solid liquid phase zone[6].

Figure 1(a) presents the possible phase-constitution combination for pseudo-binary MCEAs. The solid lines mean that the corresponding MCEAs have been successfully prepared, including disordered FCC/ordered BCC (B2)-structured[7], ordered FCC (L1$_2$)/ordered BCC (B2)-structured[8,9], FCC/Laves-structured[10], BCC/B2-structured[11], and BCC/Laves-structured[12] MCEAs. Among them, FCC/B2-structured and L1$_2$/B2-structured MCEAs, e.g., AlCoCrFeNi$_{2.1}$, Al$_{0.95}$CoFeNi$_{2.05}$, and Al$_{18}$Co$_{30}$Cr$_{10}$Fe$_{10}$Ni$_{30}$W$_2$, etc., possess both

high strength and large ductility derive from the synchronous plastic deformation, while all the rest ones show brittle fracture behaviors at room temperature[7-9,13].

It is surprising to find that disordered FCC/disordered BCC-structured MCEAs have not been designed till now. By consulting the binary phase-diagram handbooks, it is hard to single out simple eutectic alloys as structural materials. Even though the following eutectic reaction: L → FCC solid solution + BCC solid solution exists in several systems, such as Co-Cr, Cr-Ni, Cr-Cu, Cr-Pd, and Cr-Pt intermetallic compounds, e.g., Cr_3Co_2, Ni_2Cr, $CrPd$, and Cr_3Pt will form accordingly below the corresponding eutectic temperatures and thus, weaken the alloys. For instance, in the Cr-Cu binary system, both eutectic phases (Cr-rich and Cu-rich solid-solution phases) are stable below the eutectic temperature, but the eutectic point ($Cr_{1.6}Cu_{98.4}$) is very close to the Cu component, leading to a very small volume fraction of the Cr-rich phase and subsequent limited application. The above findings account for the rareness of FCC + BCC eutectic alloys.

Considering the combination of alternating soft FCC and hard BCC phase

contributes to excellent and balanced mechanical properties, it is meaningful to explore novel FCC + BCC eutectic alloys. Based on above, the purpose of this study is to locate disordered FCC/BCC-structured MCEAs and explore their microstructures and mechanical behaviors.
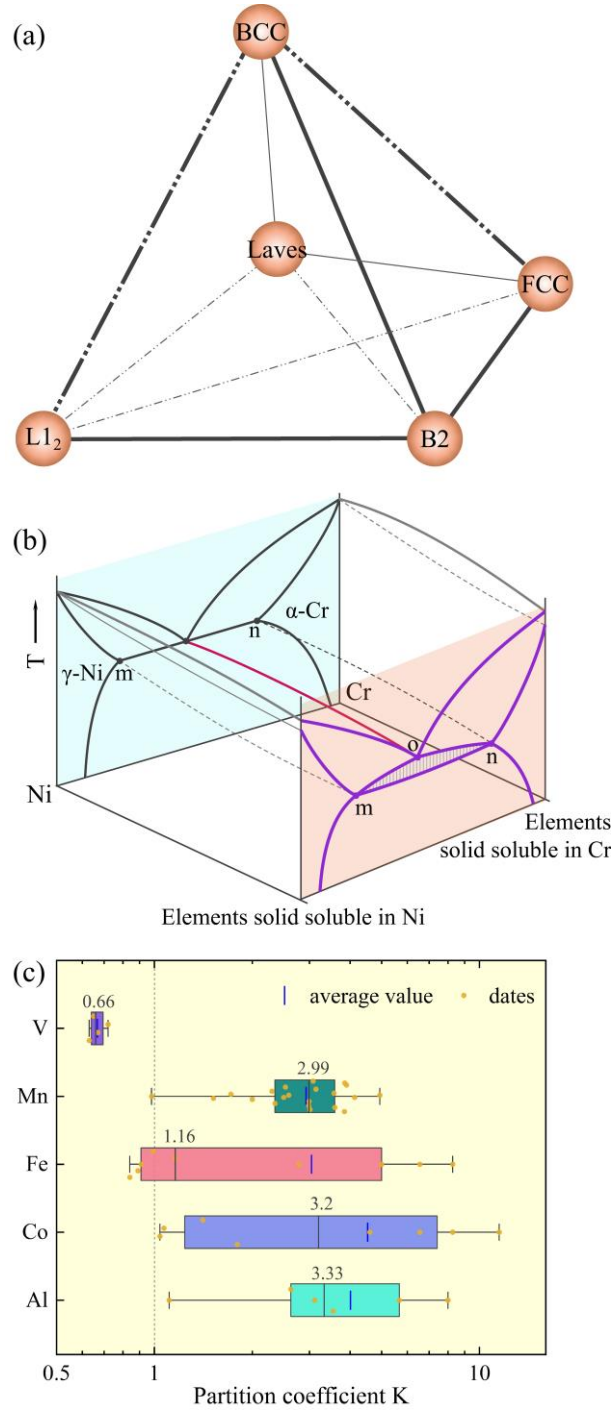
Fig. 1(a) Possible phase constitution combination for pseudo-binary MCEAs, the solid (dot-dashed) lines mean that the corresponding MCEAs have (not) been reported; (b) Schematic diagram for designing disordered FCC/BCC-structured MCEAs; (c) Elemental partition coefficient K of Cr, Ni-containing alloys[14-22], showing the V partition to BCC phase, whereas the Al, Co, Fe, and Mn partitions to FCC solid solution.

2. Methods and experiments

2.1 Design method：extend binary to multicomponent eutectics

In the present work, we aim to design FCC/BCC-structured MCEAs with 4 or more principal elements. To achieve this goal, we propose a strategy of heavily adding at least two elements into binary or ternary eutectic alloys. It is believed that appropriate elements will dissolve into both eutectic phases without largely changing the eutectic structure. Furthermore, a large number of alloying elements cause a high mixing entropy value and thus, stabilize the solid-solution eutectic phases. Here, we select Ni$_{46}$Cr$_{54}$ (at.%) eutectic as the research object, which is composed of the γ-Ni (FCC structure) and α-Cr (BCC structure) phases. The schematic diagram of our design method is shown in Fig. 1(b). The red line is called an univariant line or melting groove and possesses the three-phase equilibrium: L → α-Cr + γ-Ni. It is worth noting that the isothermal eutectic transition may change to a non-isothermal process when the component number is equal to or greater than three.

Considering that the alloying effect varies with adding elements and

concentrations, we first classify common elements into four groups according to binary phase diagrams:

I. Elements considerably dissolved in both γ-Ni and α-Cr: Al, Co, Fe, Ga, Mn, Re, Sb, and V;

II. Elements considerably dissolved only in γ-Ni: Cu, Pd, Pt, Rh, Zn, and Ge;

III. Elements considerably dissolved only in α-Cr: Ru;

IV. Elements scarcely dissolved in both Ni and α-Cr: Mg, Mo, Nb, Pb, Si, Sn, Ta, Ti, W, and Zr.

Evidently, the elements with high solubility in both γ-Ni and α-Cr solutions can be heavily added, i.e., the elements in group I are ideal candidates for alloying in $Ni_{46}Cr_{54}$ eutectic alloy. Even though the elements in group II and III can largely dissolve in γ-Ni or α-Cr phases, the finite solubility in one phase in turn limits the solubility in the other one to ensure the same chemical potentials. Therefore, the elements in group II and III can only be added in small amounts. As for the elements in group IV, a small addition will lead to the formation of a

third phase. It is supposed that adding appropriate elements may even result in the formation of triple-phase eutectic alloys.

After selecting appropriate alloying elements, another question is the assessment for elemental partitioning behavior. Here, the elements dissolve more in γ-Ni than α-Cr phases are defined as γ-Ni stabilizers and vice versa. Partition coefficient K can be used to quantitatively describe the elemental partitioning behavior in γ-Ni and α-Cr phases, and is expressed as

$$K_i = \frac{C_i^{\gamma}}{C_i^{\alpha}} \tag{1}$$

where K_i is the partition coefficient of ith element, C_i^{γ} and C_i^{α} are the concentration of ith element in γ-Ni and α-Cr phase, respectively.

The statistical K values are plotted in Fig. 1(c). The top and bottom limits of the boxes represent the 25th and 75th percentiles, the caps represent the minimum and maximum values, and the vertical line in each data set represents the median. The boxplot graph shows a wide dispersion of K values for Al (1-8), Co (1-11), Fe (0.8-8), and Mn (1-5), while V shows a small dispersion. Thus, the median is used to describe K values. In this work, the partition coefficient K of Al, Co, Fe,

Mn, and V are approximately adopted as 3, 3, 1, 3, and 0.7 respectively, indicating Al, Co, Fe, and Mn dissolve more in γ-Ni solutions, while V is a α-Cr stabilizer[14-22].

In dual-phase eutectic alloys, the phase fractions are always constant in equilibrium. Here, it is assumed that the eutectic phases fraction keeps roughly unchanged when adding solute elements. Therefore, after adding alloying elements, the predicted eutectic alloys satisfy the following equation:

$$\left(C_{Cr} + \sum_{i=1}^{n}\frac{C_i}{K_i+1}\right):\left(C_{Ni} + \sum_{i=1}^{n}\frac{K_i \cdot C_i}{K_i+1}\right) = 54:46 \qquad (2)$$

where C_{Cr} and C_{Ni} are the corresponding content of Cr and Ni, K_i is the partition coefficient of ith element besides Cr and Ni, C_i is the content of ith element in the predicated alloy, and 54 and 46 are the mole fraction of Cr and Ni in $Cr_{54}Ni_{46}$ binary eutectic alloy. It should be pointed out that the eutectic point of Cr-Ni system seems to be not identical according to literatures. Both $Cr_{54}Ni_{46}$ and $Cr_{56}Ni_{44}$ eutectic alloys have been reported[23,24]. So, we prepared the above two alloys by arc-melting and confirmed that the real eutectic point is $Cr_{54}Ni_{46}$. Based on Equation (2), several predictions of FCC/BCC-structured eutectic

alloys are listed in Table 1, in which the four predicted ternary dual-phase

eutectic alloys have been proved to be near-eutectic alloys by ternary or

pseudo-binary phase diagrams[25-29]. To further verify the validity of this design

strategy for multicomponent alloys, three quaternary alloys and one quinary alloy

will be prepared by arc-melting. If the four alloys deviate from eutectic

composition, we can locate the real eutectic point by changing relative content of

Cr and Ni elements, because Cr and Ni are strong BCC and FCC stabilizer,

respectively. The microstructure, crystal structure and plastic deformation

behavior are studied systematically in the current work.

Table 1 Prediction of FCC/BCC-structured eutectic alloys.

No.	Types	Predictions	Eutectic alloys	Deviation of Cr (%)	References
3-1	ternary	$Cr_{52}Ni_{39}Co_{10}$	$Cr_{52}Ni_{38}Co_{10}$	0	[25,26]
3-2	ternary	$Cr_{48}Ni_{42}V_{10}$	$Cr_{46}Ni_{44}V_{10}$	-2	[25,27]
3-3	ternary	$Cr_{49}Ni_{41}Fe_{10}$	$Cr_{53}Ni_{37}Fe_{10}$	+4	[25,28]
3-4	ternary	$Cr_{39}Ni_{31}Fe_{30}$	$Cr_{45}Ni_{25}Fe_{30}$ $Cr_{40}Ni_{30}Fe_{30}$	+6 +1	[25] [29]
4-1	quaternary	$Cr_{46}Ni_{34}Co_{10}V_{10}$	$Cr_{41}Ni_{39}Co_{10}V_{10}$	-5	Current work
4-2	quaternary	$Cr_{43}Ni_{37}Fe_{10}V_{10}$	$Cr_{37}Ni_{43}Fe_{10}V_{10}$	-6	Current work
4-3	quaternary	$Cr_{47}Ni_{33}Co_{10}Fe_{10}$	$Cr_{47}Ni_{33}Co_{10}Fe_{10}$	0	Current work
5-1	quinary	$Cr_{43}Ni_{33}Co_8Fe_8V_8$	$Cr_{39}Ni_{37}Co_8Fe_8V_8$	-4	Current work

2.2 Experimental methods

In this work, all ingots (each of 30 g) were prepared using vacuum arc-melting furnace. Elements of block Co, Cr, Fe, Ni and V with purity higher than 99.95 wt.% were used as raw materials. The electrolytic vanadium was melted to the block in advance to avoid splashing during melting. In order to ensure microstructure uniformity and avoid composition segregation, the melting process was repeated five times, each lasting two minutes.

The microstructures were analyzed by scanning electron microscope (SEM, Merlin Compact). The chemical compositions and element distribution were detected using an energy dispersive spectrometer attached to SEM (SEM-EDS). The SEM samples were treated by mechanical polishing, and then etched by using dilute hydrochloric acid. The crystal structure of all the alloys were characterized by using a X-ray diffractometer (XRD, Bruker D8 Advance) with Cu target at a scanning speed of 6º/min. The scanning angle (2θ) was selected between 20º and 100º. The phase structure and orientation relationship were quantitatively analyzed by transmission electron microscopy (TEM) on a transmission electron microscope (TEM, JEM-F200). The TEM samples were

prepared by twin-jet electro-polisher with a mixed solution of 90% perchloric acid and 10% ethyl alcohol at -30 degrees.

The room-temperature tensile tests were conducted by a Instron 5969 testing machine under a strain rate of 10^{-3} s^{-1} and were repeated 3 times for each alloy. The gauge length, width, thickness of the tensile specimens were designed as 12.5 mm, 2 mm, and 1 mm, respectively. Nanoindentation tests were performed using the Hysitron TI Premier Nanoindenter (Bruker, Minneapolis, MN, USA) with a Berkovich tip (radius ~ 162 nm) at room temperature. A maximum load of 2,000 μN was used for phase-specific hardness measurements. During each indent, the load was linearly increased to 2,000 μN over a period of 5 s, held constant for 2 s and unloaded in 5 s.

3. Results

3.1 Microstructures and phase constitution

Microstructures of the four predicted alloys are analyzed by SEM, revealing a full eutectic structure for the $Cr_{47}Ni_{33}Co_{10}Fe_{10}$ alloy, and Cr-rich primary phase plus eutectic structure for the rest three alloys. By changing relative content of

Cr and Ni elements, the real eutectic points are accurately located, as listed in Table 1. The slight composition deviation indicates a great feasibility and reasonability for the current design method. Here, for simplicity, the four MCEAs: $Cr_{41}Ni_{39}Co_{10}V_{10}$, $Cr_{37}Ni_{43}Fe_{10}V_{10}$, $Cr_{47}Ni_{33}Co_{10}Fe_{10}$ and $Cr_{39}Ni_{37}Co_8Fe_8V_8$ are denoted as CoV, FeV, CoFe, and CoFeV alloys, respectively.

Figure 2 presents the SEM micrographs of four MCEAs, exhibiting similar alternating lamellar eutectic microstructure. High-magnification images show that large amounts of needle-like precipitates exist in dark phases except for the CoFe alloy, which are formed by the drastic reduction in the solid solubility during solidification. The SEM-EDS results listed in Table 2 reveal that the dark phases are rich in Cr, while the Ni element is enriched in bright phases. Because Cr and Ni elements are strong BCC and FCC stabilizers, respectively. Thus, it can be inferred that the bright phases are FCC phases while the dark phases possess BCC structures.
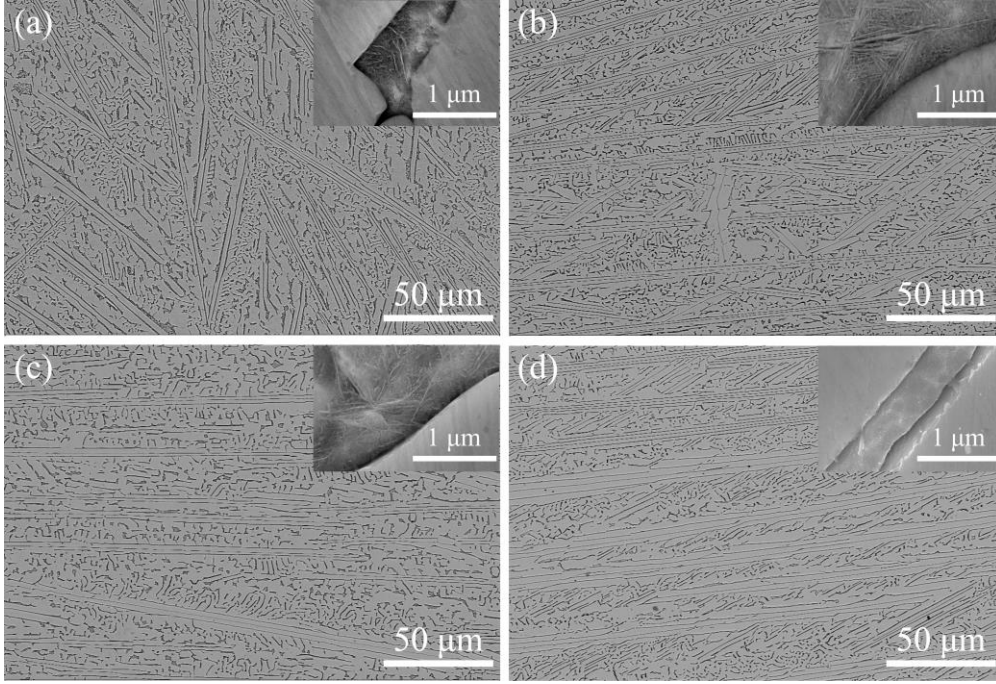
Fig. 2 SEM micrographs of four MCEAs.

(a) $Cr_{41}Ni_{39}Co_{10}V_{10}$; (b) $Cr_{37}Ni_{43}Fe_{10}V_{10}$; (c) $Cr_{39}Ni_{37}Co_8Fe_8V_8$; and (d) $Cr_{47}Ni_{33}Co_{10}Fe_{10}$.

The XRD patterns (not shown here) reveal that all the four eutectic alloys are composed of FCC and BCC phases. In addition, FCC phases have a larger phase volume fraction, in agreement with the above inference. The absence of (001) peaks for BCC phases in XRD patterns means that all the BCC phases in Co-Cr-Fe-Ni-V eutectic systems are disordered, while the BCC eutectic phases in the Al-Co-Cr-Fe-Ni family are always ordered due to the much negative mixing enthalpy of the Al-Ni combination. The approximately equal lattice constant ratios (1.2471, 1.2472, 1.2465, and 1.2446) indicate that the same orientation relationship is energetically favorable[30].

1

Due to the microstructure similarity, the TEM analysis was only conducted for $Cr_{41}Ni_{39}Co_{10}V_{10}$ and $Cr_{47}Ni_{33}Co_{10}Fe_{10}$ alloys, as presented in Fig. 3. The selected area electron diffraction (SAED) patterns near the phase boundary reveal that both the CoV and CoFe alloys have a typical Kurdjumov-Sachs orientation relationship, i.e., $[011]_{FCC}//[111]_{BCC}$, $(111)_{FCC}//(110)_{BCC}$. The SAED analysis proves that the FCC and BCC phases in both alloys are disordered, and no precipitate can be detected in the FCC matrix. As for the BCC matrix, high-resolution TEM (HR-TEM) images reveal that fine FCC precipitates exist in the BCC matrix for the CoV alloy, while no precipitate can be detected in the BCC matrix for the CoFe alloy, in agreement with the SEM results.

Table 2 Phase analysis results of the four eutectic alloys. Please add a light background color to beautify the table.

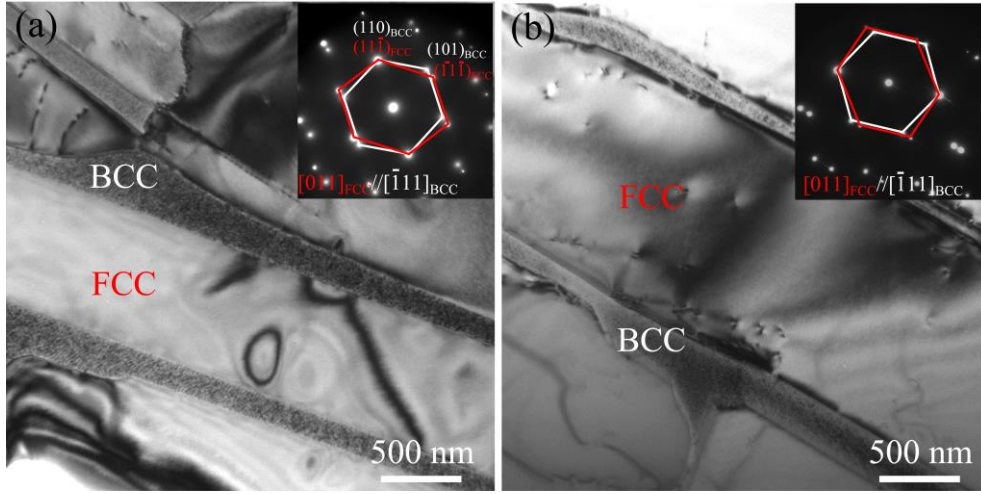| Alloys | Phases | Composition (at.%) | | | | | Lattice constant (Å) | Volume fraction (%) |
		Co	Cr	Fe	Ni	V		
$Cr_{41}Ni_{39}Co_{10}V_{10}$	FCC	10.52	37.74	-	41.93	9.82	3.5944	82
	BCC	9.70	48.84	-	30.34	11.12	2.8822	18
$Cr_{37}Ni_{43}Fe_{10}V_{10}$	FCC	-	35.67	10.13	44.84	9.36	3.6001	83
	BCC	-	44.43	9.94	33.85	11.78	2.8866	17
$Cr_{39}Ni_{37}Co_8Fe_8V_8$	FCC	8.42	37.22	8.40	38.36	7.60	3.5944	83
	BCC	7.90	47.74	7.87	27.71	8.78	2.8834	17
$Cr_{47}Ni_{33}Co_{10}Fe_{10}$	FCC	10.58	44.37	10.10	34.95	-	3.5871	86

| | BCC | 8.47 | 63.00 | 8.63 | 19.90 | - | 2.8822 | 14 |

Fig. 3 TEM bright field images of CoV and CoFe alloys, revealing typical Kurdjumov-Sachs relationships near phase boundary. (a) $Cr_{41}Ni_{39}Co_{10}V_{10}$ and (b) $Cr_{47}Ni_{33}Co_{10}Fe_{10}$.

3.2 Tensile properties

Tensile results presented in Fig. 4 indicate distinctly different tensile behaviors of the four as-cast alloys. It is obvious that the CoV alloy possesses the highest 0.2% offset yield strength ($\sigma_{0.2}$) , ultimate tensile strength (σ_{UTS}), as well as the work-hardening rate ($d\sigma/d\varepsilon$), while the CoFe alloy takes the lowest parameters. The difference between $\sigma_{0.2}$ and σ_{UTS} of both alloys reaches up to 219 and 349 MPa, respectively. It is also found that V-containing alloys possess much higher strength values than the V-free alloy, indicating that V is a better strengthening element than Cr. Figure 4(b) reveals that $d\sigma/d\varepsilon$ continues to

decrease during successive straining, demonstrating the absence of twinning-induced plasticity (TWIP) or transformation-induced plasticity (TRIP) effects during plastic deformation. The conclusion is verified by the TEM analysis.
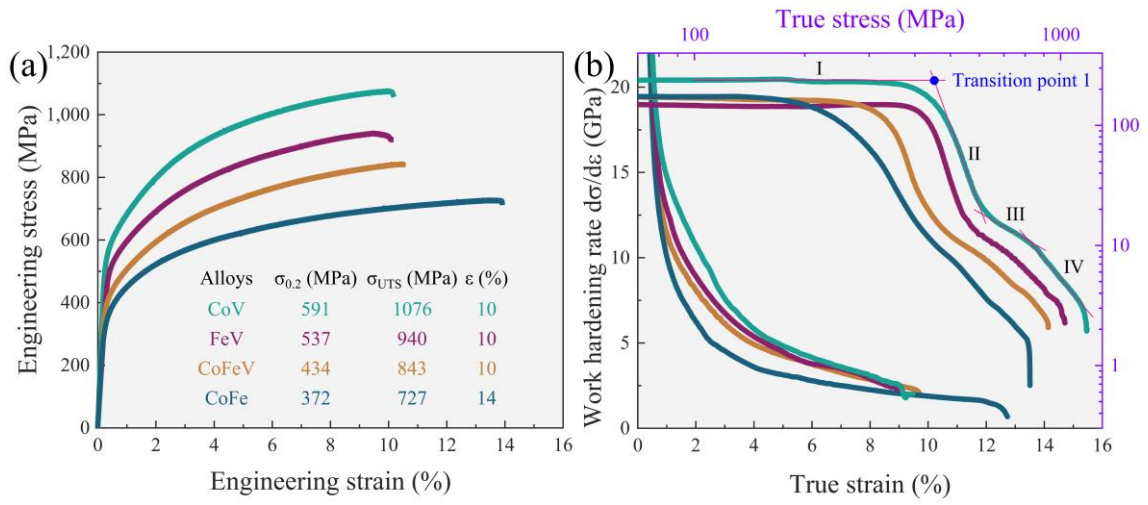

Fig. 4 Tensile results of the four as-cast eutectic alloys. (a) Tensile engineering stress-strain curves at room temperature; (b) Work-hardening rate ($d\sigma/d\varepsilon$) vs. true-strain curves, and the logarithmic graph of $d\sigma/d\varepsilon$ vs. true stress curves.

To estimate the plastic deformation more clearly, the logarithmic graph for $d\sigma/d\varepsilon$ versus σ is plotted, as displayed in Fig. 4(b). It is obvious that all the curves can be divided into four stages. In stage I, both phases deform elastically, and the transition point between stages I and II means the onset of yielding for the soft FCC matrix. Considering that the macroscopic yielding of the alloy is accompanied by dislocation motion in a considerable amount of grains, the

1

intersection of two lines paralleled to the straight part of stages I and II, denoted as transition point 1, is identified as the yield point of the FCC matrix. The corresponding FCC yield strength (σ_{FCC}), yield strain (ε_{FCC}), and permanent elongation (ε_p) on the transition point 1 are listed in Table 3. The extremely low ε_p values have the same order of magnitudes as the strains at the proportional limit or micro-yielding of SiC/Al composites[31]. The onset of the transition point 1 is independent of parameters such as the volume fraction of BCC phases (f_{BCC}) and the BCC to FCC yield strength ratio ($R^* = \sigma_{BCC}/\sigma_{FCC}$), because the BCC phases are still in an elastic state under this strain[32]. It should be emphasized that the onset of the transition point 1 is influenced by the layer size and phase distribution. Generally, a fine layer size and confined FCC phase lead to a high σ_{FCC}.

Table 3. Tensile parameters on transition point 1.

Alloys	Transition point 1		
	Stress (MPa)	Strain (%)	Permanent elongation (%)
$Cr_{41}Ni_{39}Co_{10}V_{10}$	454	0.20	0.008
$Cr_{37}Ni_{43}Fe_{10}V_{10}$	429	0.29	0.002
$Cr_{39}Ni_{37}Co_8Fe_8V_8$	331	0.12	0.003
$Cr_{47}Ni_{33}Co_{10}Fe_{10}$	254	0.16	0.010

4. Discussions

4.1 Eutectic-phase transformation in binary systems

Eutectic phase transformations commonly exist in binary or ternary systems. In order to assess the probability of eutectic transformations, we constructed a 43 × 43 matrix (see Fig. 5) containing the phase-transition types of all binary combinations of the 43 elements: alkali metal Li; alkali earth metals Be, Mg, and Ca; boron group elements B, Al, Ga, and In; carbon group elements C, Si, Ge, Sn, and Pb; nitrogen group elements Sb and Bi; oxygen group element Te; all the 3d and 4d transition metals, except Tc; and several 5d transition metals La, Ce, Gd, Hf, Ta, W, Pt, and Au.
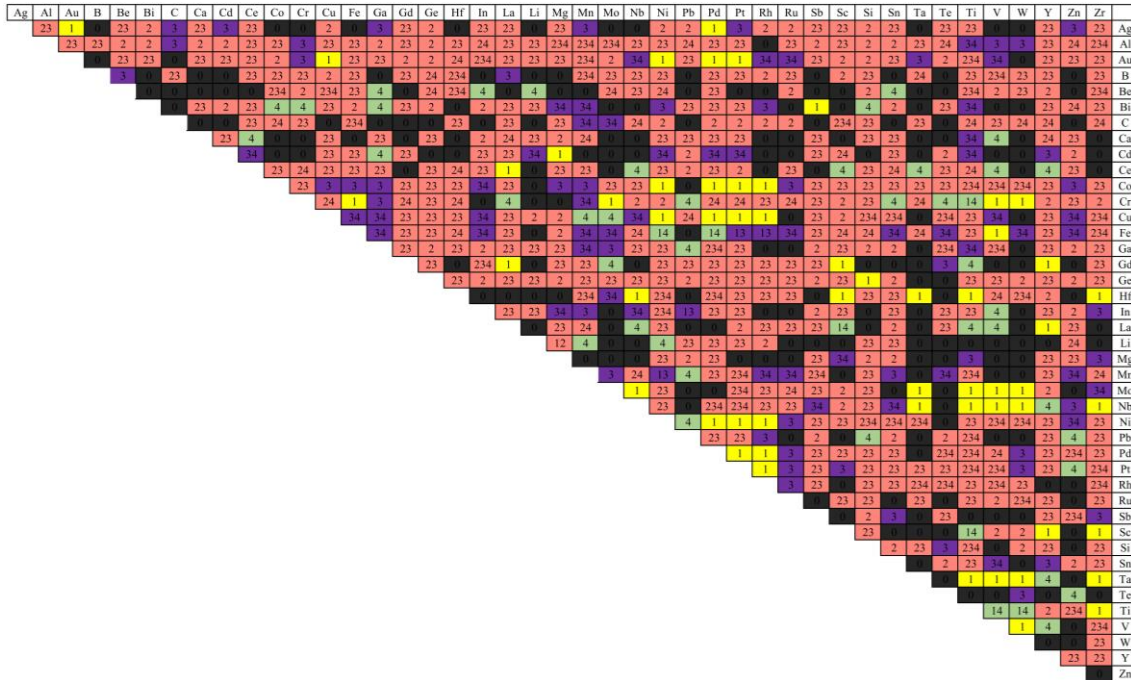
Fig. 5 Phase-transition types in binary eutectic systems. The numbers of 1, 2, 3, and 4 indicate isomorphous, eutectic, peritectic, and complex phase transition, respectively.

Because some phase diagrams have not been plotted so far, we finally obtain 685 binary phase diagrams, among which about 68 (~ 10%) are isomorphous phase diagrams, 40 (~ 6%) are complex phase diagrams (i.e., no isomorphous, eutectic or peritectic phase transformations exist in these phase diagrams), and 482 (~ 70%) contain at least one eutectic-phase transformation. The results reveal that eutectic-phase transformations commonly come into being in binary alloy systems.

Remarkably, among all the binary eutectic-phase transformations, there are only several L→FCC solid solution + BCC solid solution eutectic reactions, which exist in Co-Cr, Cr-Ni, Cr-Cu, Cr-Pd, and Cr-Pt systems. Previously, we have pointed out the rareness of FCC+BCC eutectic alloys. The main origin for this phenomenon is the formation of stable or unstable intermetallic compounds in middle of binary phase diagrams. For example, the Cr-Pt phase diagram can be divided into two pseudo-binary phase diagrams, i.e., the Cr-Cr$_3$Pt and Cr$_3$Pt-Pt pseudo-binary eutectic-phase diagrams, due to the formation of a stable Cr$_3$Pt compound phase. Another case is that eutectic phases
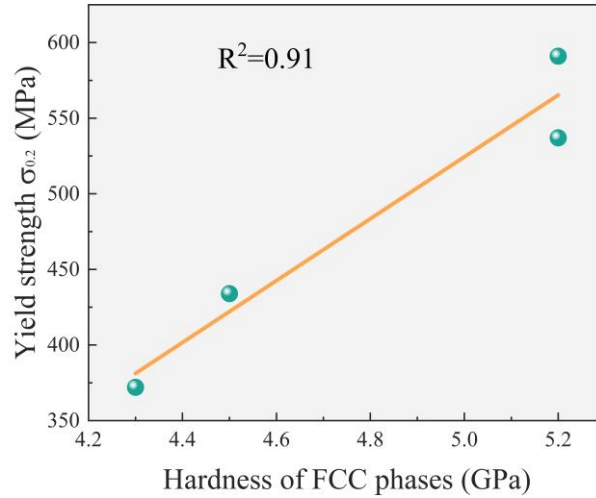
become unstable at low temperatures and transform to other metastable phases, such as in Co-Cr, Cr-Ni or Cr-Pd systems.

In the present work, we provide a novel method for designing stable multicomponent eutectic-alloy systems. It is believed that binary or pseudo-binary eutectic alloys with high solubility between component phases can be extended to multicomponent eutectic systems. So eutectic systems, such as Co-Cr and NiAl-Cr, may be good candidates for designing multicomponent eutectic systems[33]. This method indicates good potential to extend the service performance of traditional binary or ternary eutectics.

4.2 Yield-strength difference

The macroscopic yield strength, $\sigma_{0.2}$, is related with several intrinsic parameters, mainly including f_{BCC}, layer thickness, phase distribution, σ_{FCC} and $R^{*[32]}$. The SEM analysis reveals that the first three factors are similar for the four alloys. Due to the relatively small f_{BCC} (less than 20%), the majority of BCC phases are in the elastic state when the alloy is upon yielding. Therefore, $\sigma_{0.2}$ is less affected by $R^{*[34]}$. Then, we focus on the only remaining parameter, σ_{FCC}. As

discussed in part 3.2, σ_{FCC} corresponds to the stress at the transition point 1. Subtract the corresponding σ_{FCC} (listed in Table 3) from $\sigma_{0.2}$, the stress differences (137, 108, 103, and 118 MPa) are quite close to each other, suggesting that $\sigma_{0.2}$ is strongly correlated with σ_{FCC}. To prove this statement, nanoindentation tests for FCC phases are conducted to estimate the strengths of FCC phases. The results gives a clue that there is a significant positive correlation between the $\sigma_{0.2}$ and hardness of FCC phases, as presented in Fig. 6. Therefore, it is credible that the $\sigma_{0.2}$ difference originates mainly from the σ_{FCC} difference for the current four alloys.

Fig. 6 Relationship between yield strength $\sigma_{0.2}$ and the hardness of FCC phases.

4.3 Strain-hardening behavior

We first note that the engineering stress-strain curves appear not to be

parallel to each other, implying an entirely different strain-hardening behaviors. Here, classical Hollomon analysis ($\sigma = K \cdot \varepsilon^n$) is used to investigate the strain-hardening behaviors, where K is a constant, and n is referred as the strain-hardening exponent. The Hollomon parameters are determined by fitting the experimental true stress-true strain data and listed in Table 4. It is clear that all the four strain-hardening values, n, seem to be constants through the whole deformation history and are approximately the same (0.23-0.27). Since n represents the uniform deformation capacity, it can be inferred that the similar tensile elongations result from the approximately same n values.

Table 4. Hollomon parameters and measured nanoindentation hardness values.

Alloys	K	n	$\sigma_{0.2}/\sigma_{UTS}$	σ_{UTS}-$\sigma_{0.2}$ (MPa)	FCC Hardness (MPa)	BCC Hardness (MPa)	R^*
$Cr_{41}Ni_{39}Co_{10}V_{10}$	703	0.23	0.55	588	5.2	12.5	2.4
$Cr_{37}Ni_{43}Fe_{10}V_{10}$	599	0.25	0.57	488	5.2	7.4	1.4
$Cr_{39}Ni_{37}Co_8Fe_8V_8$	507	0.27	0.51	491	4.5	7.3	1.6
$Cr_{47}Ni_{33}Co_{10}Fe_{10}$	449	0.24	0.51	451	4.3	5	1.2

Excluding the impact of the yield stress, the engineering stress-strain curves in Fig. 4(a) are converted to true stress-strain curves, and the 0.2% offset yield strength is subtracted accordingly to give the portion of the flow stress associated with strain hardening, as shown in Fig. 7. The discrete curves reveal obviously

2

the distinct strain-hardening capability and can be roughly explained by the significant difference of the strain-independent K values, as listed in Table 4. Because K is related to a series of materials parameters, we next aim to explore the nature of the difference for the strain-hardening portion ($\Delta\sigma = \sigma_{flow} - \sigma_{0.2}$).
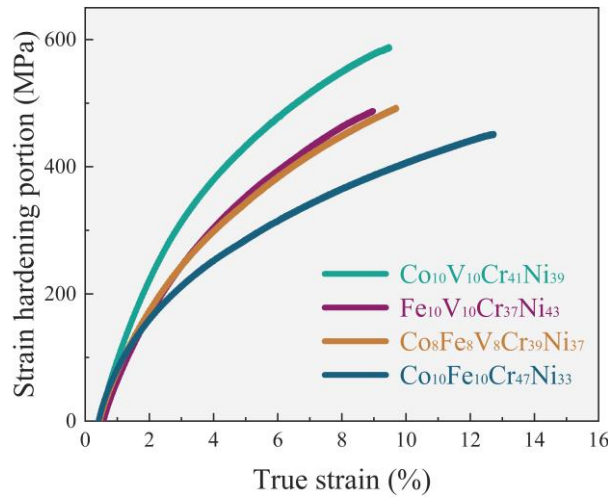

Fig. 7 Strain hardening portion ($\Delta\sigma = \sigma_{flow} - \sigma_{0.2}$) vs. true strain of the four MCEAs.

As for dual-phase eutectic alloys, the mixing rule is always adopted to describe both the yield and ultimate tensile strength, suggesting that strain hardening portion is mainly related to the intrinsic strength of eutectic phases for given systems. Therefore, the yield strength ratio, R^*, is used to estimate the strain-hardening difference. The reason for choosing this parameter is described as follows. The flow stress can be divided into two parts: the effective stress and back stress. The effective stress is the short-range stress caused by dislocation

interactions and is mainly affected by the dislocation density. Evidently, larger R^* will cause a more dislocation pile-up, higher dislocation density, and subsequent higher effective stress. The back stress is the long-range stress caused by geometrically necessary dislocations, which is associated with the plastic deformation of the grain boundary, phase boundary, and/or precipitate particles. It has been proved in many literatures that the back stress contributes greatly to the tensile flow stress of dual-phase heterogeneous materials[15,35]. As for small R^*, the stress concentration caused by the dislocation pile-up near the phase boundary easily reaches up to the critical yield stress for hard phases and leads to a small back stress. Therefore, a larger R^* benefits a higher strain-hardening capability.

To prove this trend, R^* is evaluated by nanoindentation tests. The hardness results are listed in Table 4, and the largest strain-hardening values, i.e., σ_{UTS} - $\sigma_{0.2}$, vs. R^* values are plotted in Fig. 8. The perfect linear fitting relationship indicates that the σ_{UTS} - $\sigma_{0.2}$ are strongly dependent on R^*. Therefore, it can be concluded that the strain-hardening difference for the current four MCEAs

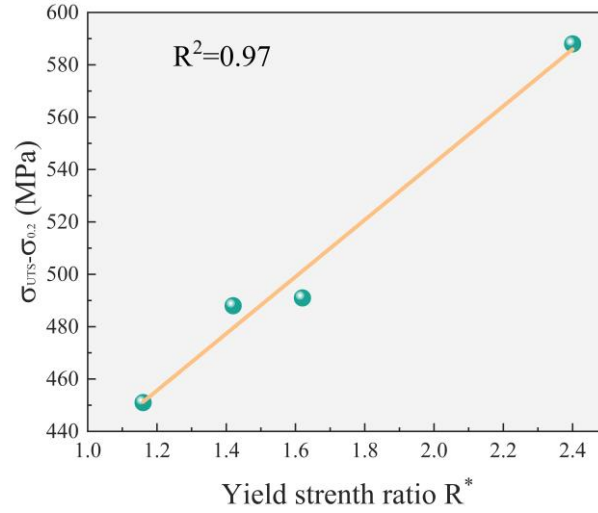originates mainly from the strength ratio of component eutectic phases.

Fig. 8 Largest train hardening value (σ_{UTS} - $\sigma_{0.2}$) vs. yield strength ratio, R^*, of the four MCEAs.

It should be emphasized that if the R^* is too large, i.e., the hard phase is too brittle, dislocation pile-up near the phase boundary will lead to a fracture along the phase boundary or within hard phases instead of the plastic deformation. This phenomenon can be found in FCC + Laves MCEAs. In another special case, both soft and hard eutectic phases are brittle whatever R^* is, e.g., for the BCC + B2 MCEA, there is no need to investigate the flow stress. Therefore, the above inference "a larger R^* benefits a higher strain-hardening capability" is only suitable for alloys consisting of both ductile phases.

5. Conclusions

In the work, we proposed a new method to design MCEAs along the univariant eutectic line. Based on this method, one quinary ($Cr_{39}Ni_{37}Co_8Fe_8V_8$) and three quaternary ($Cr_{41}Ni_{39}Co_{10}V_{10}$, $Cr_{37}Ni_{43}Fe_{10}V_{10}$, and $Cr_{47}Ni_{33}Co_{10}Fe_{10}$) MCEAs were designed and successfully prepared by arc-melting. The difference for the yield strength and strain hardening during tensile tests were investigated, and the following conclusions can be drawn.

(1) The four MCEAs exhibit entirely different tensile behaviors, with the largest strength difference occurring between $Cr_{41}Ni_{39}Co_{10}V_{10}$ and $Cr_{47}Ni_{33}Co_{10}Fe_{10}$ alloys.

(2) $Cr_{47}Ni_{33}Co_{10}Fe_{10}$ alloy possesses the highest Cr content in both the component eutectic phases, but the lowest $\sigma_{0.2}$ and σ_{UTS}, indicting V is a better strengthening element than Cr.

(3) Due to the similar microstructure, lamellar size, and volume fraction, the $\sigma_{0.2}$ difference mainly results from the yielding strength of the FCC matrix.

(4) The four as-cast alloys exhibit approximately equal strain-hardening exponents, n (0.23 - 0.27) but different strain-hardening coefficients, K. The

difference for the K and strain-hardening portion originates mainly from the strength ratio of component eutectic phases. A higher BCC/FCC strength ratio, R^*, will result in a larger strain-hardening capability.

Declaration of Competing Interest

The authors declare that they have no known competing financial interests or personal relationships that could have appeared to influence the work reported in this paper.

W911NF-19–2-0049.

References

[1] B. Cantor, I.T.H. Chang, P. Knight, A.J.B. Vincent, Microstructural development in equiatomic multicomponent alloys, Mater. Sci. Eng. A, 375-377 (2004) 213-218.

[2] J.W. Yeh, S.K. Chen, S.J. Lin, J. Y. Gan, T. S. Chin, T. T. Shun, C. H. Tsau, S. Y. Chang, Nanostructured high-Entropy alloys with multiple principal elements: novel alloy design concepts and outcomes, Adv. Eng. Mater., 6 (2004) 299-303.

[3] B. Gludovatz, A. Hohenwarter, D. Catoor, E.H. Chang, E.P. George, R.O. Ritchie, A fracture-resistant high-entropy alloy for cryogenic applications, Science, 345 (2014) 1153-1158.

[4] O.N. Senkov, G.B. Wilks, J.M. Scott, D.B. Miracle, Mechanical properties of $Nb_{25}Mo_{25}Ta_{25}W_{25}$ and $V_{20}Nb_{20}Mo_{20}Ta_{20}W_{20}$ refractory high entropy alloys, Intermetallics, 19 (2011) 698-706.

[5] Q. Zhou, S. Sheikh, P. Ou, D. Chen, Q. Hu, S. Guo, Corrosion behavior of $Hf_{0.5}Nb_{0.5}Ta_{0.5}Ti_{1.5}Zr$ refractory high-entropy in aqueous chloride solutions, Electrochem. Commun., 98 (2019) 63-68.

[6] Y.P. Lu, Y. Dong, S. Guo, L. Jiang, H. Kang, T. Wang, B. Wen, Z. Wang, J. Jie, Z. Cao, H. Ruan, T. Li, A Promising New Class of High-Temperature Alloys: Eutectic High-Entropy Alloys[J], Sci. Rep., 4 (2015) 6200.

[7] X. Jin, J. Bi, L. Zhang, Y. Zhou, X.Y. Du, Y.X. Liang, B.S. Li, A new $CrFeNi_2Al$ eutectic high entropy alloy system with excellent mechanical properties, J. Alloys Compd., 770 (2019) 655-661.

[8] Y.P. Lu, X. Gao, L. Jiang, Z. Chen, T. Wang, J. Jie, H. Kang, Y. Zhang, S. Guo, H. Ruan, Y. Zhao, Z. Cao, T. Li, Directly cast bulk eutectic and near-eutectic high entropy alloys with balanced strength and ductility in a wide temperature range[J], Acta Mater., 124 (2017) 143-150.

[9] X. Jin, Y. Zhou, L. Zhang, X.Y. Du, B.S. Li, A novel $Fe_{20}Co_{20}Ni_{41}Al_{19}$ eutectic high entropy alloy with excellent tensile properties, Mater. Lett., 216 (2018) 144-146.

[10] L. Han, X. Xu, Z.M. Li, B. Liu, C.T. Liu, Y. Liu, A novel equiaxed eutectic high-entropy alloy with excellent mechanical properties at elevated temperatures, Mater. Res. Lett., 8 (2020) 373-382.

[11] X. Chen, J.Q. Qi, Y.W. Sui, Y.Z. He, F.X. Wei, Q.K. Meng, Z. Sun, Effects of aluminum on microstructure and compressive properties of Al-Cr-Fe-Ni eutectic multi-component alloys[J], Mater. Sci. Eng. A, 681(2017) 25-31.

[12] S.G. Ma, Y. Zhang, Effect of Nb addition on the microstructure and properties of AlCoCrFeNi high-entropy alloy, Mater. Sci. Eng. A, 532 (2012) 480-486.

[13] Q. Wu, Z. Wang, X. Hu, T. Zheng, Z. Yang, F. He, J. Wang, Uncovering the eutectics design by machine learning in the Al-Co-Cr-Fe-Ni high entropy system[J], Acta Mater., 182 (2020) 278-286.

[14] J.C. Rao, H.Y. Diao, V. Ocelík, D. Vainchtein, C. Zhang, C. Kuo, Z. Tang, W. Guo, J.D. Poplawsky, Y. Zhou, P.K. Liaw, J.Th.M. De Hosson, Secondary phases in $Al_xCoCrFeNi$ high-entropy alloys: An in-situ TEM heating study

and thermodynamic appraisal, Acta Mater., 131 (2017) 206-220.

[15] X. Jin, Y.X. Liang, L. Zhang, J. Bi, Y. Zhou, B.S. Li, Back stress strengthening dual-phase $AlCoCr_2FeNi_2$ high entropy alloy with outstanding tensile properties, Mater. Sci. Eng. A, 45 (2019) 137-143.

[16] C. Jung, K. Kang, A. Marshal, K.G. Pradeep, J.B. Seol, H.M. Lee, P.P. Choi, Effects of phase composition and elemental partitioning on soft magnetic properties of AlFeCoCrMn high entropy alloys[J], Acta Mater., 171 (2019) 31-39.

[17] H. Wu, S. Huang, C. Zhu, H. Zhu, Z. Xie, Influence of Cr content on the microstructure and mechanical properties of $Cr_xFeNiCu$ high entropy alloys[J], Prog. Nat. Sci., 30 (2020) 239-245.

[18] K. Srimark, S. Dasari, A. Sharma, P. Wangyao, B. Gwalani, T. Rojhirunsakool, S. Gorsse, R. Banerjee, Hierarchical phase evolution in a lamellar $Al_{0.7}CoCrFeNi$ high entropy alloy involving competing metastable and stable phases[J], Scripta Mater., 204 (2021) 114137.

[19] E.M. Slyusarenko, A.V. Peristyi, E.Y. Kerimov, I.L. Guzei, M.V. Sofin, Ternary systems of nickel and manganese with transition metals, J. Alloy Compd, 256 (1997) 115-128.

[20] H. Li, J. Ruan, N. Ueshima, K. Oikawa, Experimental investigations of fcc/bcc phase equilibria in the Cr-Mn-Ni ternary system, Intermetallics, 127 (2020) 106994.

[21] T. Omori, J. Sato, K. Shinagawa, I. Ohnuma, K. Oikawa, R. Kainuma, K. Ishida, Experimental determination of phase equilibria in the Co-Cr-Ni system, J. Phase Equlib. Diff., 35 (2014) 178-185.

[22] S. Ueta, M. Hida, M. Kajihara, Influences of Co, Cu and V on kinetics of discontinuous precipitation in the Ni-Cr system, ISIJ Int., 53 (2013) 347-355.

[23] C. Miller, R. Field, M. Kaufman, Phase stability of γ′-Ni_2Cr and α-Cr in the Ni-Cr binary, Acta Mater., 157 (2018) 1-10.

[24] R. Kossowsky, Cellular precipitation in Ni-51Cr lamellar eutectic and cast Ni-44Cr alloys, Metall. Trans., 1 (1970) 1623-1627.

[25] P. Villars, Handbook of ternary alloy phase diagrams, A. Prince and H. Okamoto. American society for metals, (1995).

[26] P. Wang, B. Hu, X. Huang, C. Zheng, Thermodynamic assessment of the Co-Cr-Ni, Co-Cr-W and Co-Ni-W, Calphad, 73 (2021) 102252.

[27] W.M. Choi, Y.H. Jo, D.G. Kim, S.S. Sohn, S. Lee, B.J. Lee, A thermodynamic modelling of the stability of sigma phase in the Cr-Fe-Ni-V high-entropy alloy system, J. Phase Equilib. Diff., 39 (2018) 694-701.

[28] V. Raghavan, Cr-Fe-Ni (chromium-iron-nickel), J. Phase Equilib. Diff., 30 (2009) 94-95.

[29] M. Schneider, G. Laplanche, Effects of temperature on mechanical properties and deformation mechanisms of the equiatomic CrFeNi medium-entropy alloy. Acta Mater., 204 (2021) 116470.

[30] U. Dahmen, Orientation relationships in precipitation systems, Acta Metall., 30 (1982) 63-73.

[31] F. Zhang, P. Sun, X. Li, G. Zhang, An experimental study on deformation behavior below 0.2% offset yield stress in some SiC_p/Al composites and

their unreinforced matrix alloys, Mater. Sci. Eng. A, 300 (2001) 12-21.

[32] Y.O. Tomota, I. Tamura, Mechanical behavior of steels consisting of two ductile phases, Trans. Iron Steel I. Jpn., 22 (1982) 665-677.

[33] A. Shafiei, Design of eutectic high entropy alloys in Al-Co-Cr-Fe-Ni system, Met. Mater. Int. 27 (2021) 127-138.

[34] S. Neti, M.N. Vijayshankar, S. Ankem, Finite element method modeling of deformation behavior of two-phase materials Part I: stress-strain relations, Mater. Sci. Eng. A, 145 (1991) 47-54.

[35] X.L. Wu, M.X. Yang, F.P. Yuan, G.L. Wu, Y.J. Wei, X.X. Huang, Y.T. Zhu, Heterogeneous lamella structure unites ultrafine-grain strength with coarse-grain ductility, P. Natl A. Sci., 112 (2015) 14501-14505.